Exploring femtosecond laser ablation in single particle aerosol mass spectrometry

Ramakrishna Ramisetty[1*], Ahmed Abdelmonem[1], Xiaoli Shen[1], Harald Saathoff[1], Thomas Leisner[1] and Claudia Mohr[1, 2*]

[1]Institute of Meteorology and Climate Research, Karlsruhe Institute of Technology, Germany
[2]Department of Environmental Science and Analytical Chemistry, Stockholm University, Sweden

*Correspondence to: Claudia Mohr (claudia.mohr@aces.su.se)

Abstract

Size, composition, and mixing state of individual aerosol particles can be analysed in real time using single particle mass spectrometry (SPMS). In SPMS, laser ablation is the most widely used method for desorption and ionization of particle components, often realizing both in one single step. Excimer lasers are well suited for this task due to their relatively high power density (10^7 W cm^{-2}-10^{10} W cm^{-2}) in nanosecond (ns) pulses at ultraviolet (UV) wavelengths, and short triggering times. However, varying particle optical properties and matrix effects make a quantitative interpretation of this analytical approach challenging. In atmospheric SPMS applications, this influences both the mass fraction of an individual particle that gets ablated, as well as the resulting mass spectral fragmentation pattern of the ablated material. The present study explores the use of shorter (femtosecond, fs) laser pulses for atmospheric SPMS, and systematically investigates the influence of power density and pulse duration on airborne particle (polystyrene latex, SiO_2, NH_4NO_3, NaCl, and custom-made core-shell particles) ablation and reproducibility of mass spectral signatures. We used a laser ablation aerosol time-of-flight single particle mass spectrometer (LAAPTOF, AeroMegt GmbH), originally equipped with an excimer laser (wavelength 193 nm, pulse width 8 ns, pulse energy 4 mJ), and coupled it to an fs-laser (Spectra Physics Solstice-100F ultrafast laser) with similar pulse energy, but longer wavelengths (266 nm with 100 fs and 0.2 mJ, 800 nm with 100 fs and 4 mJ, respectively). Generally, mass spectra exhibit an increase in ion intensities (factor 1 to 5) with increasing laser power density (~10^8 W cm^{-2} to ~10^{13} W cm^{-2}) from ns- to fs-laser. At the same time, fs-laser ablation produces spectra with larger ion fragments and ion clusters, as well as clusters with oxygen, which does not render spectra interpretation more simple compared to ns-laser ablation. Quantification of ablated material remains difficult due to incomplete ionization of the particle. Furthermore, the fs-laser application still suffers from limitations in triggering it in a useful timeframe. Further tests are needed to test potential advantages of fs- over ns-laser ablation in SPMS.

1 Introduction

Atmospheric aerosols are known to have large impacts on climate change, air quality and human health, and these effects are strongly related to the chemical composition of individual aerosol particles (Fuzzi et al., 2015). Atmospheric aerosols are highly heterogeneous in composition, due to the vast number of natural and anthropogenic sources, as well as transformation and mixing processes during their residence time in the atmosphere (Kulkarni et al., 2011). Most analyses of aerosol chemical composition focus on the bulk, not least

Atmospheric
Measurement
Techniques
Discussions

40   due to the very small mass and number of molecules present in an average atmospheric particle, making single
particle studies challenging. However, mixing state and composition of individual particles are crucial information
for the assessment of e.g. the particles' interactions with light or water vapour, and thus their contribution to
climate change (Charles, 2012; IPCC, 2007; Jacobson, 2005; John, 2016)

Single particle mass spectrometry (SPMS) is a powerful tool for the investigation of the size-resolved chemical

45   composition of individual atmospheric aerosol particles in real time (Brands et al., 2011; Gaie-Levrel et al., 2012;
Murphy, 2007; Murphy et al., 2006; Pratt et al., 2009; Pratt and Prather, 2012; Zelenyuk et al., 2010). Single
particle mass spectrometers currently in use by different groups worldwide have closely similar designs (Gaie-
Levrel et al., 2012; Johnston, 2000; Murphy and Thomson, 1995; Zelenyuk et al., 2009). They usually consist of
one or two scattering lasers to detect the particle size by particle time-of-flight, an ionization laser, commonly a

50   nanosecond (ns) excimer laser for particle desorption and ionization in one single step, and the mass analyser
(Murphy, 2007).

Quantitative analysis of single aerosol particles via laser ablation remains challenging. Single step laser
desorption and ionization with excimer lasers is highly nonlinear (Zelenyuk and Imre, 2005). Usually, particles
are not completely ablated (Ge et al., 1996; Murphy, 2007), and the ablation process leads to irreproducible

55   spectra. The dominant yield of species with low ionization potential further limits the quantitative ability of ns-
laser SPMS (Reilly et al., 2000). The absorption of photons depends on the optical properties of the chemical
components of the particle, with important implications for core-shell or multi-component particles (Cahill et al.,
2015). Reported approaches for improvement of the quantitative abilities of SPMS include e.g. two step
vaporization-ionization, where a CO_2 laser was used prior to excimer laser ionization for the evaporation of the

60   particles (Cabalo et al., 2000), or the use of a high power density Nd:YAG laser of 5 ns pulse duration with 100
mJ pulse energy ($> 10^{10}$ W m^{-2}) (Lee et al., 2005; Mahadevan et al., 2002; Zhou et al., 2007). Lee and Mahadevan
found that the kinetic energy of ions produced from ns-laser pulses is proportional to the particle size with a power
law relationship, which influences ion detection efficiency in traditional time-of-flight mass spectrometer optics.
The interaction of a high-intensity laser beam with a solid target leads to the generation of a plasma that increases

65   its energy content, its average charge state, and its density during the pulse duration. Zhou et al. (2007) used a
one-dimensional hydrodynamic model and experimental observations to explain ns-laser pulse interactions with
particles, and observed that the laser energy absorption efficiency and thus ionization efficiency increases with
shorter pulse width (from 10 ns to 10 ps). The energy per unit volume is greater for femtosecond laser pulses
compared to nanosecond laser pulses.

70   Potential differences in the ablation mechanism and resulting single particle mass spectra as a function of pulse
duration were also a focus in our studies. Compared to ns-laser ablation, the pulse duration of ultrashort (pico-
and femtosecond, fs) laser pulses is less than the typical picosecond time range of thermal diffusion effects. Fs-
lasers are widely used in the fields of micro machining and nanoparticle ablation (Chichkov et al., 1996; Gattass
and Mazur, 2008; Malvezzi, 2014; Richard et al., 2013; Tsuji et al., 2003). Fs-laser ablation mechanisms include

75   Coulomb explosion (soft ablation) and phase explosion followed by thermal ablation (strong ablation), depending
on fs-laser intensities (Amoruso et al., 1999; Leitz et al., 2011; Zhou et al., 2007). However, ablation and
ionization of airborne (moving) particles is different from ablation of solid substrates, where the maximum amount
of pulse energy is deposited onto the substrate. Also for the widely used ns-lasers in SPMS, the ion formation
mechanism is not completely understood (Murphy, 2007). For both ns- and fs-laser, the ablated/desorbed material

80   of a particle can interact with the laser beam. The ablated particle components move ~5 μm during a 5 ns pulse or ~0.1 μm during a 100 fs pulse, respectively, and in both cases remain well within the typical laser beam width. In the case of fs-laser ablation, the higher photon density may favour multi-photon ionization, which may lead to the formation of new species from the ablated plume in the subsequent Coulomb or phase explosion.

Ultimately, the resulting mass spectral pattern in SPMS will depend on the energy transferred to the particle
85   via the ionization laser, which is related to pulse width, laser power, and wavelength. Shorter pulses exhibit e.g. higher power densities than longer pulses at the same laser energy. Higher power densities usually lead to higher ionization efficiencies, as e.g. in multiphoton interactions, where the total ion intensity is proportional to the power density of the ionization laser (Malvezzi, 2014). High-energetic, short-wavelength and short-pulse-duration ionization lasers may thus be a valid choice in single particle ionization.

In this study we compared mass spectra of atmospherically relevant airborne particles and dedicated test
90   particles from ns- and fs-laser ablation using a commercially available laser ablation aerosol time-of-flight mass spectrometer (LAAPTOF, AeroMegt Gmbh). The results presented here are an extension of the work by Zawadowicz et al. (2015), who coupled a Particle Analysis by Laser Mass Spectrometry (PALMS) with an fs-laser (Spectra Physics Solstice-100F ultrafast laser) to investigate mass spectral patterns of NaCl, NH_4NO_3, and
95   lead doped NH_4NO_3 particles. Overall, they observed similar mass spectra in both ns- and fs-laser ablation, but also showed that atoms with high ionization energy such as Cl are more easily ionized by the fs-laser due to its higher power density. At the same time, their fs–PALMS exhibited lower sensitivity to lead than the PALMS employing the ns-laser.

To achieve a better understanding of fs-laser ablation in SPMS, we systematically obtained mass spectra of
100   particles of different size and chemical composition for both ns- and fs-laser ionization. Furthermore, we varied the power density of the ionization lasers by varying the laser energy, and laser wavelength in the case of fs-laser (800 and 266 nm), and by changing the focus positions of the lasers. We describe qualitative and quantitative differences of the mass spectra obtained, and discuss implications of our results for the quantitative abilities of the LAAPTOF, and SPMS in general.

105   **2 Methodology**

2.1 LAAPTOF

The LAAPTOF has been described already in several other publications (Ahern et al., 2016; Gemayel et al., 2016; Marsden et al., 2016, 2017; Reitz et al., 2016; Zawadowicz et al., 2017; Shen et al.) and therefore we will focus
110   here especially on those aspects related to its operation with the fs laser. The LAAPTOF consists of four major modules: an aerodynamic lens focusing incoming particles into a narrow beam, the sizing section with two ultraviolet (UV) 405 nm continuous wave detection laser diodes (DL1, DL2) set 11.3 cm apart from each other, the laser ablation/particle ionization region, and a bipolar time-of-flight mass spectrometer (Fig. 1). In the sizing region, the time delay between the detection of the scattered laser light of DL1 and DL2 by photomultiplier tubes
115   (PMT, Thorn EMI, UK, type 9781R) is used to calculate the size of particles in the range of 200 - 2500 nm. The scattering signal from DL2 produces a 10 V transistor–transistor logic (TTL) electronic signal that triggers the 193 nm ns excimer laser (ArF, pulse width of 5 - 8 ns, adjustable pulse energy from 0 - 10 mJ, ATLEX-S, ATL Lasertechnik GmbH). The excimer laser shoots at the particle and at the same time triggers the data acquisition system with a 5 V TTL electronic signal. The laser beam is slightly defocused at the position (about 1 cm from

120   focus position) in order to increase the particle-laser interaction surface, and the beam diameter is ~ 300 µm where it encounters the aerosol particle (F2, Fig. 1). The focus position is at 20 cm from the lens, and ionization happens 2 - 4 cm after the focus position. The laser beam produces both positive and negative ions, which are deflected into the corresponding time-of-flight regions of the bipolar mass spectrometer. Typically, each particle hit by the excimer laser generates a positive and negative mass spectrum each.

125   **2.2 fs-laser coupled LAAPTOF**

The fs-laser (Spectra Physics Solstice-100F ultrafast laser) we coupled to the LAAPTOF is a Ti:Sapphire source, emitting pulses of 800 nm radiation with 1 kHz. Pulse duration is ~100 fs. The laser beam profile is close to Gaussian with a beam quality factor $M^2 < 1.3$ ($M^2 = 1$ for an ideal Gaussian beam). The maximum pulse energy

130   is ~3.5 mJ. In this work, the peak power density (calculated as the power per beam area at focal point) is varied by changing the pulse energies. Excimer (ns-) and fs-laser beam parameters as well as pulse energies and corresponding peak power densities at focus points F1 and F2 (see below) are listed in Tables 1 and 2.

For the coupling of the fs-laser with the LAAPTOF, a few technical changes were necessary. Fig. 1 also includes a schematic of the modified LAAPTOF. Since it was not possible to trigger the fs-laser, it was running

135   in free firing mode with a frequency of 1 kHz. To only record spectra from when a particle was hit by the fs-laser, the scattered light from the fs-laser interaction with the particle detected by the second set of PMT was used to trigger the data acquisition. This and the fact that scattered light of the high-power fs-laser could be detected by the PMT (yielding false particle size information) meant that both detection lasers were futile, and thus switched off. This led to absence of size information. To avoid loss of spectral signal due to the delay of ~10 µs between

140   triggering and the start of data acquisition, data acquisition was run in pre-trigger mode (Fig. 2).

A movable focusing lens set-up was used for multiple focusing positions between F2 (20 cm from the focusing lens towards the inlet) and F1 at ~1 cm further towards inlet, to better understand the effect of power density on mass spectral patterns (insert in Fig. 1). The power densities at F2 are ~1.5 times higher than at F1.

2.3 Particle types and experiments

145

For comparison of mass spectral patterns and signal intensities of fs- and ns-laser ablation in the LAAPTOF, we chose the following particle samples: monodisperse polystyrene latex (PSL) particles, core-shell particles with a gold core and shells of silver (Ag), silica (SiO_2), and poly(allylamine hydrochloride) (PAH), salts (NaCl, NH_4NO_3), and spherical silica (SiO_2) particles. The sample details are tabulated in Table 3. All samples were

150   dissolved or diluted in nano pure water (18 MΩ), nebulized (Topas ATM 221, Topas AG), and then dried with silica driers (Topas AG). The dried aerosol particles were size-selected with a differential mobility analyser (DMA 3080, TSI) and sent to the LAAPTOF.

All samples were measured with different laser power densities corresponding to different energies for both ns- and fs-lasers (Table 2). Per sample and laser type and setting, we tried to record spectra from at least 500

155   particles (see Table S1 and S2 in the supplementary information, SI). Empty spectra were excluded in the data analysis.

3 Results and Discussion

3.1 Qualitative differences between ns- and fs-laser spectra

160   In the following, the qualitative differences between ns- and fs-laser positive and negative mass spectra are compared for typical pulse energies (4 mJ in the ns-laser and 3.2 mJ in the fs-laser, respectively).

3.1.1 PSL particles

165   A comparison of typical mass spectra of individual PSL particles with a geometric diameter (d_p) of 500 nm for ns- and fs-LAAPTOF are shown in Fig. 3. The positive ns-laser spectrum consists of series of carbon clusters C_n^+ (n=1–7) and hydrogenated carbon clusters $C_nH_m^+$ (n = 1–7, m = 1–3) with different intensities ($\pm$ 10 %) for different single particles. The insert in Fig. 3a shows the clusters with 5 carbon atoms. All other carbon clusters have similar numbers of hydrogen atoms. The negative ns-spectrum exhibits generally lower signal intensity and

170   consists only of three major C_n^- (n = 1 – 3) and $C_nH_m^-$ (m = 1–2) peaks.

With the fs-laser (800 nm, similar results for 266 nm, not shown), a total of ~ 500 particle spectra were recorded. From these 500 particles, 54 % are of type 1 (Fig. 3c-d), and 42 % of type 2 (Fig. 3e-f), respectively. Type 1 consists of series of positive and negative C_n^+, $C_nH_m^+$ (n=1–8, m=1–2), C_n^- and $C_nH_m^-$ (n=2–8, m=1–2) ions. The positive spectrum also exhibits signal at m/z 18 and 16, which we assign to H_2O^+ and O^+, potentially

175   from residual water. The insert in Fig. 3c shows the clusters with 5 carbon atoms ($C_5H_m^+$, m = 0–2). The ion patterns are similar for positive ion clusters with different carbon atom numbers. Type 2 spectra consist of a longer series of carbon-containing clusters C_n^+ and $C_nH_m^+$ (n=1–15, m=1–2) in positive mode. Signal intensity is lower in negative mode, with shorter carbon cluster series C_n^- (n=2–3). The type 1 spectra show more negative ion clusters than the type 2 spectra, whereas type 2 shows more positive ion clusters. One explanation for this

180   observation could be that the type 2 spectra are generated from particles that are ionized closer to the positive extraction region, whereas the type 1 spectra may arise from particles ionized closer to the negative extraction region or in the middle of the ionization region of the mass spectrometer.

In both laser ablation methods we observe formation of carbon clusters and hydrogenated carbon cluster ions from PSL particles. For fs-laser ablation, larger carbon clusters (> 7 carbon atoms) with (in positive mode) fewer

185   hydrogen atoms (< 3 hydrogen atoms) are observed. This may be due to the higher power density of the fs-laser, and reactions of the primary ion species with the source plume forming larger clusters as secondary products (Zaidi et al., 2010). The increase in number of larger clusters with increasing laser pulse energy was also observed for ns-laser PSL spectra (Weiss et al., 1997).

3.1.2 NaCl particles

190

Bipolar mass spectra of NaCl particles of an electrical mobility diameter (d_m) of 400 nm for ns- and fs-laser are shown in Fig. 4. The positive ns-laser spectrum consists of atomic sodium and molecular ions (Na^+, Na_2^+), and Na_2Cl^+ and $Na_3Cl_2^+$ ions. The negative ion spectrum consists of chlorine ions (Cl^-, Cl_2^-), and sodium chloride cluster ions ($NaCl_2^-$, $Na_3Cl_2^-$). The bipolar spectrum is representative of 55% of a total of 600 particles. The

195   remaining spectra are empty or contain no partial features of NaCl.

From the fs-LAAPTOF measurements (800 nm, similar results for 266 nm, not shown) ~ 80 single particle spectra were considered for analysis. The rest out of ~ 500 spectra are empty. A representative single particle bipolar spectrum is shown in Fig. 4c-d. The positive spectrum consists of Na^+, Na_2^+, Cl^+, Na_2Cl^+, $NaCl_2^+$, $Na_3Cl_2^+$, NaO_2^+ ions, and H^+, O_2^+ ions most likely from residual water. The negative spectrum consists of Na^-, Na_2^-, Cl^-,

200   Cl_2^-, Na_2Cl^-, $Na_2Cl_3^-$, and $Na_4Cl_4^-$ ions. Around 20 % of particles exhibited ~ 10 % less intense signal of $Na^{+/-}$ and $Na_2^{+/-}$, while the signal of the other ions was similar across the spectra.

The qualitative difference between ns- and fs-LAAPTOF spectra is the presence of Cl^+ and Na_2^+ ions in positive, and Na_2^- and Cl_2^- ions in negative fs-spectra, which are not commonly observed in ns-spectra. In addition, NaO_2^+ and NaO_2^{2+} ions (O likely from residual water) are present in the positive spectrum of the fs-LAAPTOF.

205   Zawadowicz et al (2015) reported ions with similar combinations of Na and Cl in their fs-PALMS single particle spectra, but no NaO clusters. The dissociation energy of the NaCl molecule is 4.26 eV, thus smaller than the ionization energy of Na^+ (5.13 eV) and Cl^+ (12.96 eV). The electron affinity of Na^- and Cl^- is 0.52 eV and 2.35 eV, respectively (Sansonetti and Martin, 2005). In the case of ns-laser ablation with lower power density, NaCl can easily dissociate and form Na^+ and Cl^- ions. For Cl^+ ion formation, twice as much energy (12.96 eV) is

210   required, available during the fs-laser ablation process. Ionization energies are even higher for molecular Na and Cl, as well as for doubly charged Na and Cl ions. We also observed more cluster ions in the fs-laser spectra (Na_2Cl^+, $NaCl_2^+$, Na_2Cl^-, $Na_2Cl_3^-$ and $Na_4Cl_4^-$) compared to the ns-laser spectra, which again indicates a more complex ionization mechanism during fs-laser ablation.

3.1.3 NH₄NO₃ particles

215

The positive and negative mass spectra of NH_4NO_3 particles with $d_m = 400$ nm for ns- and fs-LAAPTOF are shown in Fig. 5. The ns-laser spectrum is representative of 500 particles. The positive spectrum consists of NH_2^+/O^+, OH^+, NH_4^+, NO_2^{2+}, NO^+, NO_2^+, and NO_3^+ ion signatures, while the negative spectrum contains N^{2-}, NH_2^- /O^-, OH^-, NH_4^-, NO_2^{2-}, NO^-, O_2^-, NO_2^-, NO_3^-, and $HNO_3NO_2^-$ ions.

220   The fs-LAAPTOF bipolar spectrum represents only 10 % of a total of 500 spectra. The majority of the particles was poorly hit and/or ionized. The positive spectrum contains H^+, N_2^+, $(NH_4)_2^+$, and $(NH_4)_3^+$ ions in addition to the ions observed in the ns-LAAPTOF positive spectrum, however there is no NO_3^+ signature. There is much lower (two orders of magnitude) signal intensity in the negative spectrum compared to the positive spectrum. Only ~1 % of negative fs-laser spectra exhibit significant signal (panel d), with peaks from N^{2-}, N_2^-, NO^-, O_2^-, and NO_2^-

225   ions, with albeit lower sensitivity.

The ns-LAAPTOF bipolar spectrum is comparable to the ammonium nitrate single particle spectrum obtained by the PALMS (Zawadowicz et al., 2015). NH_4NO_3 predominantly leads to positive ions (NH_2^+/O^+, OH^+, NH_4^+, NO_2^{2+}, NO^+, and NO_2^+ are the most intense peaks). Clear signal was observed with the ns-LAAPTOF for the $HNO_3NO_2^-$ ion, in accordance with observations with an on-line laser desorption/ionization (LDI) mass

230   spectrometer with excimer laser wavelength 193 nm (Neubauer et al., 1998), but in contradiction to observations with the PALMS (Zawadowicz et al., 2015) or the real-time single-particle mass spectrometer (RSMS) with excimer laser wavelength 193 nm (Reinard and Johnston, 2008). The fs-LAAPTOF positive spectrum consists of $N_xO_y^+$ (x = 0-2, y = 0-2), $(NH_4)_x^+$, where x = 1-3, H^+, and N_2^+ ions. The ionization energies of $(NH_4)_x^+$ (for x > 1) cluster ions are very high (Dunlap and Doyle, 1996), which may be the reason for the absence of these ions in the

235   ns-spectra.

3.1.4 SiO₂ particles

Mass spectra of individual SiO_2 particles of $d_p = 1000$ nm measured by ns- and fs-LAAPTOF are shown in Fig. 6. A bipolar spectrum of SiO_2 particles, representative of about 80% of 860 spectra from ns-LAAPTOF obtained

Atmospheric
Measurement
Techniques
Discussions

240   with 4 mJ pulse energy is presented in panels a and b. The positive spectrum consists of Si^+ and SiO^+ ions, the negative spectrum contains O^-, SiO_2^-, and SiO_3^- ions. The other 20 % of spectra have three more $Si_xO_y^-$ clusters (x = 2-3, y = 4-5).

       Recent studies with a LAAPTOF by Marsden et al. (2016) of silicate (SiO_4) rich ambient sea spray particles featured similar mass spectral peaks, namely from Si^+, SiO^+, and O^-, SiO^-, SiO_2^- ions. Single particle

245   characterization studies of SiO_2 rich particles by Cahill et al. (2015) with an Aerosol Time-of-Flight Mass Spectrometer (ATOFMS) using a 266 nm Nd:YAG ionization laser also produced O^-, SiO_2^-, and SiO_3^- ions. Both studies presented similar spectra to the ones shown in Fig. 6a – b. Another ambient single particle study with a PALMS powered with an excimer laser (193 nm, ~4 mJ pulse energy) by Gallavardin et al. (2008) showed Si_xO_y negative ion clusters (x = 1-2, y = 1-4), similar to the peaks in 20 % of spectra from our LAAPTOF (not shown

250   here). Another experimental study of silica clusters with a 308 nm XeCl excimer laser coupled time-of-flight mass spectrometer observed clusters of silica $(SiO_2)_n^-$ units (n = 1-6) (Xu et al., 2000).

       The fs-LAAPTOF bipolar spectra for silica are shown in Fig. 6c – d, representative of ~ 80 % of 530 particles. The positive spectrum consists of O^+, Si^+, O_2^+, $Si_xO_y^+$ (x = 1-3, y = 2x+1), and $Si_xO_y^+$ (x = 1-2, y= x+1) ions, the negative spectrum of O^-, Si^-, O_2^-, $Si_xO_y^-$ (x = 1-6, y = 2x+1), and $Si_xO_y^-$ (x = 1-2, y = x+1) ions. To our knowledge

255   there are no studies on fs-laser ablation of individual silica particles, we thus cannot compare our spectra with other single particle spectra. Kato et al. (2007) investigated fs- and ns-laser ablation of silica substrates, and silicon-rich solutions. They observed positive silicon clusters, Si_x^+ (x = 1-6) and claimed that ns-laser ablation leads to more fragmentation, whereas fs-laser ablation leads to better atomization with elemental ionization. With fs-laser ablation of silicon substrate, clusters of Si^+_n (n = up to 10) have been observed (Bulgakov et al., 2004).

260   The major difference between the positive ns-LAAPTOF and fs-LAAPTOF spectra is the existence of elemental oxygen (O^+, O_2^+), and silica clusters (SiO_2^+, $Si_2O_3^+$, $Si_2O_5^+$, and $Si_3O_7^+$) in the fs-laser spectra. In the negative fs-laser spectra, O^- and Si^- elemental ions as well as $Si_xO_y^-$ (x = 1-6, y = 2x+1) and $Si_xO_y^-$ (x=1-2, y= x+1) cluster ions are observed. Only O^-, SiO_2^-, and SiO_3^- ions are also common in ns-laser negative spectra. Another major difference is the high intensity of signal in the fs-LAAPTOF spectra. Overall, fs-laser ablation

265   yields more elemental information (positive silicon and positive oxygen), but also leads to higher-order clusters than ns-laser ablation.

       Since the SiO_2 is bonded covalently in nature, high energies are required to break it. Consequently, we observe both cations and anions of SiO_2 constituents in the fs-spectra. The 266 nm UV fs-LAAPTOF spectra of SiO_2 particles contain similar spectral features, but less intense signal than the 800 nm fs-laser spectra.

270   **3.1.5 Gold-silver core-shell particles**

       A bipolar single particle mass spectrum of gold-silver core-shell particles from ns-LAAPTOF is shown in panels a and b of Fig. 7. This bipolar spectrum represents 27 % of a total of 850 particles or spectra. The peaks below 100 Th are fragments from the surfactant Cetyl-trimethylammonium bromide (CTAB), $C_{19}H_{42}BrN$, which was

275   used to stabilize the gold-silver particles in the suspension. The positive spectrum consists of signal from the two silver isotopes $Ag^{(107,109)+}$, of Au^+, and AuO^+. The negative spectrum contains signal from $Ag^{(107,109)-}$, Au^-, silver oxide isotopes $AgO_2^{(139,141)-}$, and also silver dioxide $(AgO_2)^-$. About 43 % of the 850 spectra contain only signal from elemental silver and silver oxides, and no gold peaks. The remaining 30 % of single particle spectra consist only of signal from CTAB.

280   The respective fs-LAAPTOF bipolar spectrum is shown in Fig. 7c-d, which is representative of 19 % of ~ 1500 particles. The positive spectrum consists of signal from the surfactant CTAB, elemental silver isotopes $Ag^{(107,109)+}$, and silver oxide isotopes $Ag^{(139,141)+}$. The negative spectrum is almost empty, with very small peaks of silver and silver oxide, and none of the fs-LAAPTOF spectra contains gold signal. 8 % of the negative fs-LAAPTOF spectra have clear signal from the surfactant and very small silver peaks.

285   The gold-silver particles contain a 300 nm gold core (nearly 67 % of total the weight percentage with 2.18 pg of mass), and a 150 nm thick shell of silver (about 33 % of the total mass percentage with 1.08 pg of mass). The ns-LAAPTOF mass spectral signatures, however, feature higher signal for silver than for gold. More signal from both core and shell is observed when there is less surfactant signal in the ns-spectra. The major difference between ns-LAAPTOF and fs-LAAPTOF spectra is the absence of gold peaks in the fs- spectra. At the wavelength of the

290   excimer ns-laser (193 nm), the reflectance of both gold and silver are nearly 35 % (Kah et al., 2015). At the wavelength of the fs-laser (800 nm), the reflectance is more than 95% for both gold and silver. The high reflectance of gold in the IR likely leads to reduced ablation of the core.

        The existence of gold and silver oxides in both ns- and fs-laser spectra is indicative of laser plume interactions with background or residual water. Systematic studies on humidity effects on mass spectra of single particles may

295   explain more about this type of oxides, like e.g. the studies by Neubauer et al. (1998).

3.1.6 Gold-Poly(allylamine hydrochlorid) core-shell particles

The second type of of core-shell particles we tested for mass spectral comparison between ns- and fs-laser is made of a gold core (d_p = 300 nm) and an organic polymer (poly (allylamine hydrochloride), PAH) shell (coating

300   thickness = 50 nm). Ns- and fs-LAAPTOF spectra are shown in Fig. 8.

        The ns-LAAPTOF bipolar spectrum (panels a and b) is representative of 44 % of totally 450 particles. It features signal from the organic PAH shell (elemental carbon $C_n^{+/-}$, and hydrocarbons $C_nH^{+/-}$), as well as elemental gold ($Au^{+/-}$) ions. The remaining 66 % of spectra mainly consist of signal from the PAH shell, and exhibit no or almost no signal from the gold core.

305   Two types of fs-LAAPTOF spectra are shown in panels c-f. The spectra are representative of 10 and 15 % of the total number of spectra (1000), respectively. Spectra that do not contain gold or PAH signal are excluded, as are spectra that contain only background signal peaks (Ar^+, CO_2^+). Fig. 8c-d is representative of a spectrum that contains distinctive signal from the gold core, and C_n^+ ions as well as $C_nH_n^+$ cluster ions. The second type (panels e-f) does not exhibit any signal from the gold core, and also less signal from the carbon clusters.

310   The comparison of ns- and fs-LAAPTOF spectra of gold-PAH core-shell particles reveals more signal from carbon clusters, which are similar to the peaks from PSL particles, in the fs-spectra. Signal from the gold core was only observed in one of a total of 1000 particles, again due to the low absorption of gold in the IR (Manca et al., 2007; Pereira et al., 2015). The spectra of gold-PAH particles from the 266 nm fs-LAAPTOF (not shown) also did not exhibit signal from the gold core, and only low signal intensity from the PAH shell.

315   The third type of core-shell particles, Au-SiO$_2$, produced mass spectra and no signal from the gold core at both fs-laser wavelengths (Fig. S1). Signal from the gold core was again observed in the ns-laser spectra. They contained Si, SiO, SiO$_2$ positive ions, as well as hydrocarbon ions from the surfactant, and negative hydrocarbon, elemental carbon, and oxygen signal from the SiO$_2$ shell.

Atmospheric
Measurement
Techniques
Discussions

3.2 Signal intensity as a function of laser power density and particle size

3.2.1 Signal intensity variation with laser power density

We investigated the relationship between ion signal intensity and laser power density for all particle samples. The increase in power density from the lowest (0.8 mJ) to the highest (8 mJ) excimer laser pulse energy corresponds to one order of magnitude ($3.2*10^8 – 3.2*10^9$ W cm^{-2}). For the fs laser, the energy was varied from 0.3 mJ to 3.5 mJ, corresponding to more than one order of magnitude difference in power density. Due to the large spectrum-to-spectrum variance, average signal intensities per power density settings were calculated for 10 mass spectra representative of the typical spectra discussed in section 3.1 (cf. Fig. S2).

The mass spectra generated with the fs-laser have on average a factor of 5 higher total ion intensity compared to those generated with the ns-laser. Average signal intensity versus power density for both ns- and fs-lasers and focus positions F1 and F2 is shown in Fig. 9. All samples exhibit an increase in average signal intensity (by a factor of up to 5, depending on particle type) with increasing ns- or fs-laser (800 nm) power at F1. The exception is NaCl, which seems to be more efficiently ionized (compare section 3.1.2) at the higher power densities of the fs-laser compared to the ns-laser, albeit with a saturation effect. The observed slight saturation effect of signal intensity at higher power densities for both lasers may be due the coulombic repulsion among the ions during multiphoton ionization, observed as well by L'Huillier et al. (1987).

The power density of the laser acting on the particles depends on the position of the focus relative to the particles, and it will be higher (by a factor of ~ 1.5) closer to focus postion (F2) than further away from the focus (F1). This corresponds to a difference of a factor of 2 for the average ion intensities.

3.2.2 Ion signal intensity variation with particle size

To explore the quantitative abilities of the fs- and ns-laser we also investigated the average ion signal intensity variation as a function of laser power density with respect to particle size (subplots a and b in Fig. 10), using PSL particles of 500 and 1000 nm diameter. Similar subplots (Fig. 10c – d) are shown for focus position F1. The total ion signal is significantly larger (factor ~2 – 7) for larger PSL particles. The lowest difference was observed for the fs-laser generated spectra, which exhibited almost no dependency on power density. The largest differences were obtained for lower laser power densities of the ns-laser. The mass ratio of the two particle sizes is a factor of ~ 8, much larger than the relative differences in the total ion intensities. The increase in ion signal thus does not scale linearly with the difference in mass of the two particles sizes and of the material potentially to be ablated. Similar effects were also observed by Reents (1994) for RbNO$_3$ and (NH$_4$)$_2$SO$_4$ particles. This demonstrates the quantitative limitations of both ns- and fs-laser ablation. .

4 Conclusions

We coupled the commercially available single particle mass spectrometer LAAPTOF, originally equipped with an ns excimer laser, with a free firing fs-laser to investigate mass spectral patterns and signal intensity for a variety of atmospherically relevant aerosol particles and dedicated test particles. For the fs-laser application, data were obtained with pre-triggering data acquisition mode. Particle types sampled (and their diameter) include PSL particles (500 nm, 1000 nm), NaCl (400 nm), NH$_4$NO$_3$ (400 nm), Silica (1000 nm), and gold-silver, gold-SiO$_2$, and gold-PAH core-shell particles (600 nm, 400 nm, and 400 nm, respectively).

Atmospheric
Measurement
Techniques
Discussions

360   Overall, mass spectral signatures for ns-and fs-laser ablation and different particle types are fairly similar. Generally, ns-laser spectra for the same particle type exhibit higher reproducibility than fs-laser spectra. This likely because the ns-laser can be triggered, which leads to some limitation of the physical extent of the potential interaction region of particle and laser beam, which is not the case for the free firing fs-laser. Qualitative differences between fs- and ns-laser spectra vary depending on particle type. Larger clusters (C_nH_m clusters with

365   n > 7 for PSL particles, or higher order SiO_2 clusters) were e.g. observed in the higher power density fs-laser spectra. The existence of such larger clusters in the fs-laser spectra can potentially be assigned to the formation of the new molecules during the Coulomb or phase explosion of the fs-laser ablation process. We find that these large clusters in fs-laser spectra do not necessarily improve the quantitative abilities of SPMS. For NaCl particles, only in fs-laser spectra high ionization energy species like $Cl^{+/-}$ or N^+ were detected. Fs-laser ablation also led to

370   formation of oxides (for e.g. core-shell particles, silica particles, and silver oxides for the gold-silver core-shell particles).

Apart from differences in ionization process, also laser wavelength and particle optical properties play an important role in SPMS, especially important for core-shell particles or inhomogeneously mixed particles. This

375   became apparent for the core-shell particles with their gold core. Gold is highly reflective at a wavelength of 800 nm, thus no gold signal was observed in the fs-laser spectra. Generally, fs-laser generated mass spectra show a factor of 1 to 5 higher total ion intensities compared to those from the ns-laser.

Variation in power density does not have a large impact on mass spectral patterns for both laser types, but

380   influences ions signal intensity. The average ion signal intensity is increased by a factor of 2 - 5 for an increase in laser power density by at least one order of magnitude for both laser modes. Ion signal intensity also shows an (albeit non-linear) dependency on particle size, as tested for PSL particles with diameters of 500 and 1000 nm. This non-linearity would warrant further investigation for these instruments to improve their quantitative abilities. The smaller impact of particle size on ion signal intensity for the fs-laser compared to the ns-laser system observed

385   here indicates that fs-lasers might not be the most effective way to improve SPMS quantification.

Based on our study we conclude that fs-lasers do not represent a simple or efficient way forward in the improvement of the quantitative abilities of SPMS in atmospheric research. Further tests are needed to investigate potential the advantages of fs- over ns-laser ablation in atmospheric SPMS. High energetic (~100 mJ) nanosecond lasers may potentially be a better choice than high power density fs-lasers due to the operational ease and cost.

390

Data availability
Data will be provided upon request by the authors.
Author contributions

395   R.R. set up the experiment, did the measurements, analysed the data and wrote the manuscript. A.A. operated the femtosecond laser system and did the optical coupling. X.S. helped with the setup. H.S., T.L., and C.M. developed the scientific approach, and supported the experimental procedures and data analysis. R.R., H.S., and C.M. developed the manuscript. All co-authors participated in scientific discussions on the interpretation of the results.
Acknowledgements

Atmospheric
Measurement
Techniques
Discussions

Open Access

EGU

Competing interests

405   The authors declare that they have no conflicts of interest.

References

Amoruso, S., Bruzzese, R., Spinelli, N., and Velotta, R.: Characterization of laser-ablation plasmas, Journal of Physics B: Atomic, Molecular and Optical Physics, 32, R131, 1999.

410 Brands, M., Kamphus, M., Böttger, T., Schneider, J., Drewnick, F., Roth, A., Curtius, J., Voigt, C., Borbon, A., Beekmann, M., Bourdon, A., Perrin, T., and Borrmann, S.: Characterization of a Newly Developed Aircraft-Based Laser Ablation Aerosol Mass Spectrometer (ALABAMA) and First Field Deployment in Urban Pollution Plumes over Paris During MEGAPOLI 2009, Aerosol Sci Tech, 45, 46-64, 2011.

Bulgakov, A. V., Ozerov, I., and Marine, W.: Silicon clusters produced by femtosecond laser ablation: non-
415 thermal emission and gas-phase condensation, Applied Physics A, 79, 1591-1594, 2004.

Cabalo, J., Zelenyuk, A., Baer, T., and Miller, R. E.: Two-Color Laser Induced Evaporation Dynamics of Liquid Aerosols Probed by Time-of-Flight Mass Spectrometry, Aerosol Science and Technology, 33, 3-19, 2000.

Cahill, J. F., Fei, H., Cohen, S. M., and Prather, K. A.: Characterization of core-shell MOF particles by depth profiling experiments using on-line single particle mass spectrometry, Analyst, 140, 1510-1515, 2015.

420 Charles, K.: Chemistry and Composition of Atmospheric Aerosol Particles, Annual Review of Physical Chemistry, 63, 471-491, 2012.

Chichkov, B. N., Momma, C., Nolte, S., von Alvensleben, F., and Tünnermann, A.: Femtosecond, picosecond and nanosecond laser ablation of solids, Applied Physics A, 63, 109-115, 1996.

Dunlap, B. I. and Doyle, R. J.: Ammonium Nitrate Cluster Ions, The Journal of Physical Chemistry, 100, 5281-
425 5285, 1996.

Fuzzi, S., Baltensperger, U., Carslaw, K., Decesari, S., Denier van der Gon, H., Facchini, M. C., Fowler, D., Koren, I., Langford, B., Lohmann, U., Nemitz, E., Pandis, S., Riipinen, I., Rudich, Y., Schaap, M., Slowik, J. G., Spracklen, D. V., Vignati, E., Wild, M., Williams, M., and Gilardoni, S.: Particulate matter, air quality and climate: lessons learned and future needs, Atmos. Chem. Phys., 15, 8217-8299, 2015.

430 Gaie-Levrel, F., Perrier, S., Perraudin, E., Stoll, C., Grand, N., and Schwell, M.: Development and characterization of a single particle laser ablation mass spectrometer (SPLAM) for organic aerosol studies, Atmos. Meas. Tech., 5, 225-241, 2012.

Gallavardin, S. J., Froyd, K. D., Lohmann, U., Moehler, O., Murphy, D. M., and Cziczo, D. J.: Single Particle Laser Mass Spectrometry Applied to Differential Ice Nucleation Experiments at the AIDA Chamber, Aerosol Sci
435 Tech, 42, 773-791, 2008.

Gattass, R. R. and Mazur, E.: Femtosecond laser micromachining in transparent materials, Nat Photon, 2, 219-225, 2008.

Ge, Z., Wexler, A. S., and Johnston, M. V.: Multicomponent Aerosol Crystallization, Journal of Colloid and Interface Science, 183, 68-77, 1996.

440 IPCC: Climate change 2007: The physical science basis, Cambridge University Press, New York, NY, 2007.

Jacobson, M. Z.: Fundamentals of Atmospheric Modeling, Cambridge University Press, Cambridge, 2005.

John, S.: Atmospheric Chemistry and Physics: From Air Pollution to Climate Change. 2016.

Johnston, M. V.: Sampling and analysis of individual particles by aerosol mass spectrometry, J Mass Spectrom, 35, 585-595, 2000.

445 Kah, P., Rajan, R., Martikainen, J., and Suoranta, R.: Investigation of weld defects in friction-stir welding and fusion welding of aluminium alloys, International Journal of Mechanical and Materials Engineering, 10, 26, 2015.

Atmospheric
Measurement
Techniques
Discussions

Kato, T., Kobayashi, T., Matsuo, Y., Kurata-Nishimura, M., Oyama, R., Matsumura, Y., Yamamoto, H., Kawai, J., and Hayashizaki, Y.: Comparison between femtosecond and nanosecond laser ablation of solution samples applied on a substrate, Journal of Physics: Conference Series, 59, 372, 2007.

450 Kulkarni, P., Baron, P. A., and Willeke, K.: Introduction to Aerosol Characterization. In: Aerosol Measurement, John Wiley & Sons, Inc., 2011.

L'Huillier, A., Jönsson, L., and Wendin, G.: Multiphoton ionization of many-electron atoms, International Journal of Quantum Chemistry, 31, 833-840, 1987.

Lee, D., Park, K., and Zachariah, M. R.: Determination of the Size Distribution of Polydisperse Nanoparticles 455 with Single-Particle Mass Spectrometry: The Role of Ion Kinetic Energy, Aerosol Science and Technology, 39, 162-169, 2005.

Leitz, K.-H., Redlingshöfer, B., Reg, Y., Otto, A., and Schmidt, M.: Metal Ablation with Short and Ultrashort Laser Pulses, Physics Procedia, 12, 230-238, 2011.

Mahadevan, R., Lee, D., Sakurai, H., and Zachariah, M. R.: Measurement of Condensed-Phase Reaction Kinetics 460 in the Aerosol Phase Using Single Particle Mass Spectrometry, The Journal of Physical Chemistry A, 106, 11083-11092, 2002.

Malvezzi, A. M.: Laser–Matter Interaction in LIBS Experiments. In: Laser-Induced Breakdown Spectroscopy: Theory and Applications, Musazzi, S. and Perini, U. (Eds.), Springer Berlin Heidelberg, Berlin, Heidelberg, 2014.

Manca, L., Boštjan, J., Danilo, S., and Rok, K.: In situ synthesis of Ag nanoparticles in polyelectrolyte multilayers, 465 Nanotechnology, 18, 325601, 2007.

Marsden, N., Flynn, M. J., Taylor, J. W., Allan, J. D., and Coe, H.: Evaluating the influence of laser wavelength and detection stage geometry on optical detection efficiency in a single-particle mass spectrometer, Atmos. Meas. Tech., 9, 6051-6068, 2016.

Murphy, D. M.: The design of single particle laser mass spectrometers, Mass Spectrometry Reviews, 26, 150-165, 470 2007.

Murphy, D. M., Cziczo, D. J., Froyd, K. D., Hudson, P. K., Matthew, B. M., Middlebrook, A. M., Peltier, R. E., Sullivan, A., Thomson, D. S., and Weber, R. J.: Single-particle mass spectrometry of tropospheric aerosol particles, Journal of Geophysical Research: Atmospheres, 111, n/a-n/a, 2006.

Murphy, D. M. and Thomson, D. S.: Laser Ionization Mass Spectroscopy of Single Aerosol Particles, Aerosol 475 Science and Technology, 22, 237-249, 1995.

Neubauer, K. R., Johnston, M. V., and Wexler, A. S.: Humidity effects on the mass spectra of single aerosol particles, Atmospheric Environment, 32, 2521-2529, 1998.

Pereira, S. O., Trindade, T., and Barros-Timmons, A.: Biotinylation of optically responsive gold/polyelectrolyte nanostructures, Gold Bulletin, 48, 3-11, 2015.

480 Pratt, K. A., Mayer, J. E., Holecek, J. C., Moffet, R. C., Sanchez, R. O., Rebotier, T. P., Furutani, H., Gonin, M., Fuhrer, K., Su, Y., Guazzotti, S., and Prather, K. A.: Development and Characterization of an Aircraft Aerosol Time-of-Flight Mass Spectrometer, Anal Chem, 81, 1792-1800, 2009.

Pratt, K. A. and Prather, K. A.: Mass spectrometry of atmospheric aerosols—Recent developments and applications. Part II: On-line mass spectrometry techniques, Mass Spectrometry Reviews, 31, 17-48, 2012.

485 Reilly, P. T. A., Lazar, A. C., Gieray, R. A., Whitten, W. B., and Ramsey, J. M.: The Elucidation of Charge-Transfer-Induced Matrix Effects in Environmental Aerosols Via Real-Time Aerosol Mass Spectral Analysis of Individual Airborne Particles, Aerosol Science and Technology, 33, 135-152, 2000.

Atmospheric
Measurement
Techniques
Discussions

Open Access

Reinard, M. S. and Johnston, M. V.: Ion Formation Mechanism in Laser Desorption Ionization of Individual Nanoparticles, Journal of the American Society for Mass Spectrometry, 19, 389-399, 2008.

490   Richard, E. R., Xianglei, M., Jhanis, J. G., and Jong-Hyun, Y.: Femtosecond vs. nanosecond laser pulse duration for laser ablation chemical analysis, Spectroscopy, 28, 2013.

Sansonetti, J. E. and Martin, W. C.: Handbook of Basic Atomic Spectroscopic Data, Journal of Physical and Chemical Reference Data, 34, 1559-2259, 2005.

Tsuji, T., Kakita, T., and Tsuji, M.: Preparation of nano-size particles of silver with femtosecond laser ablation in
495   water, Applied Surface Science, 206, 314-320, 2003.

W. D. Reents, J., Downey, S. W., Emerson, A. B., Mujsce, A. M., Muller, A. J., Siconolfi, D. J., Sinclair, J. D., and Swanson, A. G.: Real-time compositional analysis of submicrometre particles, Plasma Sources Science and Technology, 3, 369, 1994.

Weiss, M., Verheijen, P. J. T., Marijnissen, J. C. M., and Scarlett, B.: On the performance of an on-line time-of-
500   flight mass spectrometer for aerosols, Journal of Aerosol Science, 28, 159-171, 1997.

Xu, C., Long, Y., Qian, S., and Li, Y.: The generation mechanism of silicon oxide–aluminum oxide compound clusters by laser ablation of siliceous materials, Microporous and Mesoporous Materials, 39, 351-358, 2000.

Zaidi, A. A., Hu, A., Wesolowski, M. J., Fu, X., Sanderson, J. H., Zhou, Y., and Duley, W. W.: Time of flight mass spectrometry of polyyne formation in the irradiation of liquid alkanes with femtosecond laser pulses, Carbon,
505   48, 2517-2520, 2010.

Zawadowicz, M. A., Abdelmonem, A., Mohr, C., Saathoff, H., Froyd, K. D., Murphy, D. M., Leisner, T., and Cziczo, D. J.: Single-Particle Time-of-Flight Mass Spectrometry Utilizing a Femtosecond Desorption and Ionization Laser, Analytical Chemistry, 87, 12221-12229, 2015.

Zelenyuk, A. and Imre, D.: Single Particle Laser Ablation Time-of-Flight Mass Spectrometer: An Introduction to
510   SPLAT, Aerosol Science and Technology, 39, 554-568, 2005.

Zelenyuk, A., Imre, D., Earle, M., Easter, R., Korolev, A., Leaitch, R., Liu, P., Macdonald, A. M., Ovchinnikov, M., and Strapp, W.: In Situ Characterization of Cloud Condensation Nuclei, Interstitial, and Background Particles Using the Single Particle Mass Spectrometer, SPLAT II, Anal Chem, 82, 7943-7951, 2010.

Zelenyuk, A., Yang, J., Choi, E., and Imre, D.: SPLAT II: An Aircraft Compatible, Ultra-Sensitive, High Precision
515   Instrument for In-Situ Characterization of the Size and Composition of Fine and Ultrafine Particles, Aerosol Sci Tech, 43, 411-424, 2009.

Zhou, L., Park, K., Milchberg, H. M., and Zachariah, M. R.: Understanding the Interaction of an Intense Laser Pulse with Nanoparticles: Application to the Quantification of Single Particle Mass Spectrometry, Aerosol Science and Technology, 41, 818-827, 2007.

520

525

Atmospheric
Measurement
Techniques
Open Access

Discussions

Table 1: Laser parameters of ns- and fs-lasers. λ = wavelength, E= energy per pulse, τ = pulse duration, P (avg) = average power per pulse.

530

Parameter	Type	λ (nm)	E (mJ)	τ	f (Hz)	P(avg) W	Beam dimensions (mm)
Excimer –ns Laser	ArF	193	0 - 10	~5-8 ns	Max 300	2.4	24
fs- Laser	Ti:sapphire	800	~3.5	~100 fs	1000	>3.5	7

Table 2: Excimer ns-laser and fs-laser pulse energies and corresponding power densities at focus positions F1 and F2.

Laser Type	Excimer ns-UV Laser (193nm)			fs-UV (266nm)	fs-IR (800nm)			
Energy (mJ)	0.8	4.0	8.0	0.2	0.3	1.7	3.2	3.5
Peak power density at F1 (W cm^{-2})	2.15×10^8	1.07×10^9	2.15×10^9	2.69×10^{12}	4.03×10^{12}	2.28×10^{13}	4.3×10^{13}	4.7×10^{13}
Peak power density at F2 (Wcm^{-2})	3.2×10^8	1.6×10^9	3.2×10^9	4.0×10^{12}	6.1×10^{12}	3.4×10^{13}	6.5×10^{13}	7.1×10^{13}

535 **Table 3: Particle samples used in this study. The samples marked by an asterisk were originally polydisperse, and size-selected through a DMA. d_m = electrical mobility diameter; d_p= geometric diameter.**

Sample	Vendor	Size d_p (nm)
PSL500	Thermo Scientific®, USA	500
PSL800	Thermo Scientific®, USA	800
PSL1000	Thermo Scientific®, USA	1000
NaCl	Merck KGaA	400*
NH$_4$NO$_3$	Merck KGaA	400*
SiO$_2$	Palas AG	1000
Au-Ag	Nanopartz Inc, USA	600 (300 nm core and 150 nm thick shell)
Au-PAH	Nanopartz Inc, USA	400 (300 nm core and 50 nm thick shell)
Au-SiO$_2$	Nanopartz Inc, USA	400 (300 nm core and 50 nm thick shell)
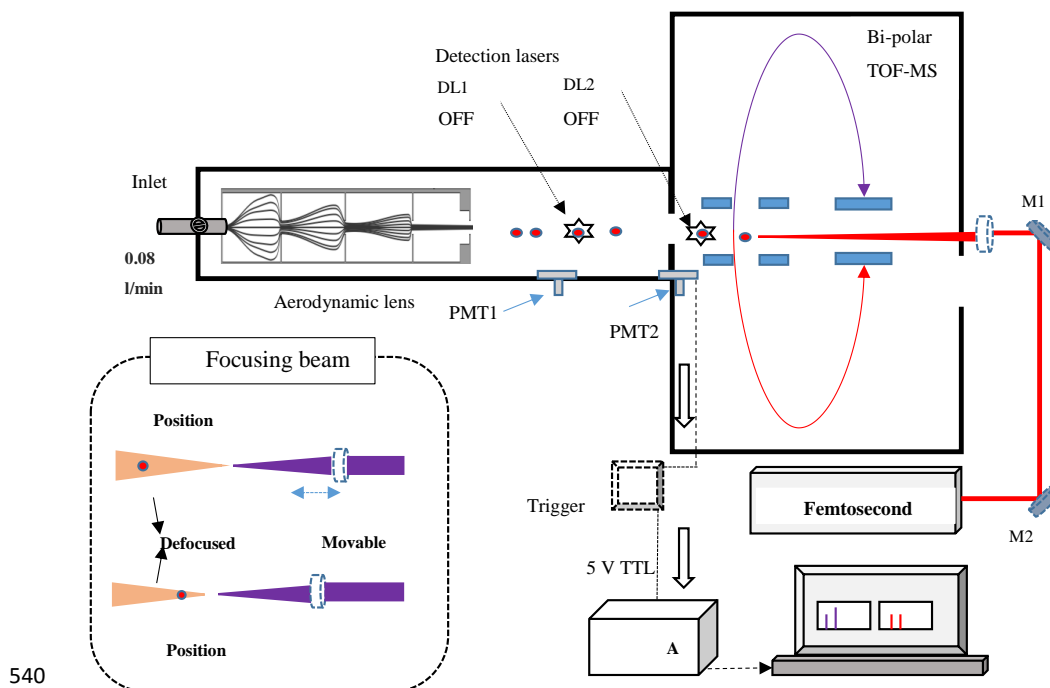
Figure 1: Schematic diagram of the LAAPTOF coupled with the fs-laser. The detection lasers DL1 and DL2 are turned off, as well as the first set of PMT (PMT1). PMT2 collects the scattered light from the interaction of the fs-laser with the particle. The PMT2 signal is connected to the trigger box and produces a trigger with a 5 V TTL signal for the ADC data acquisition. The corresponding spectra of each ablated particle are recorded and stored in the computer. The insert picture shows the variation in focus position between F1 and F2 using a movable lens (L). M1, M2 are mirrors. (Not to the exact scale).
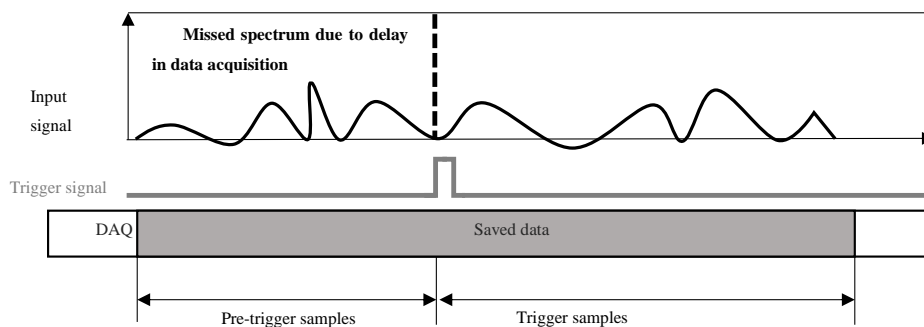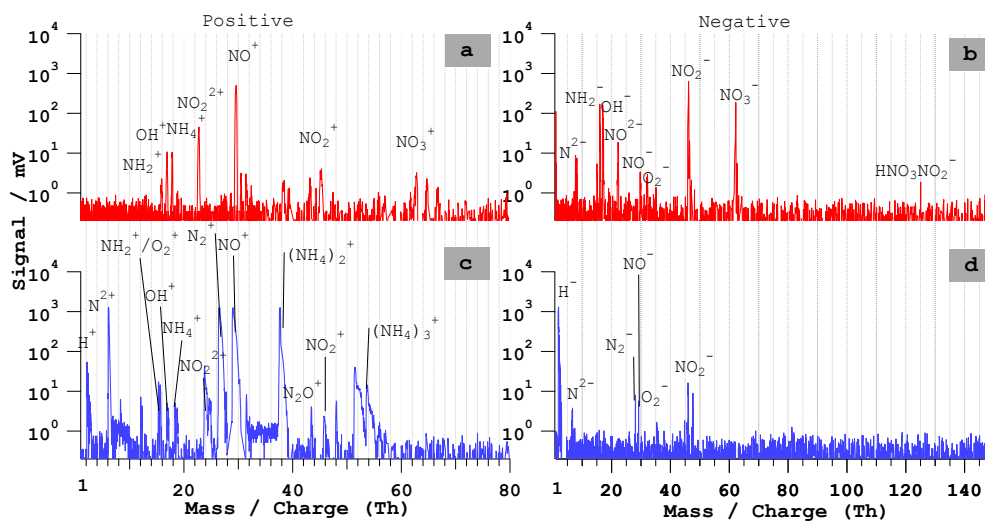

Figure 2: Pre-trigger sampling mechanism of the data acquisition system. The data arriving before the trigger event (pre-trigger samples) are saved in the temporary memory of the data acquisition card and then combined with the trigger samples.

F*igure* 3: Bipolar mass spectra of single PSL particles of d_p = 500 nm. a – b: Typical ns-laser spectra; c – d: fs-laser (λ = 800 nm) spectra for 54 % of particles; e –f: fs-laser (λ = 800 nm) spectra for 42 % of particles.

560   **Figure 4:** Bipolar mass spectra of NaCl single particles of d_m = 400 nm. a – b: Typical ns-laser spectra; c – d: fs-laser (λ = 800 nm) spectra.

Figure 5: Bipolar mass spectra of NH₄NO₃ particles of d_P= 400 nm. a – b: Typical ns-LAAPTOF spectra; c – d: fs-LAAPTOF (λ = 800 nm) spectra.
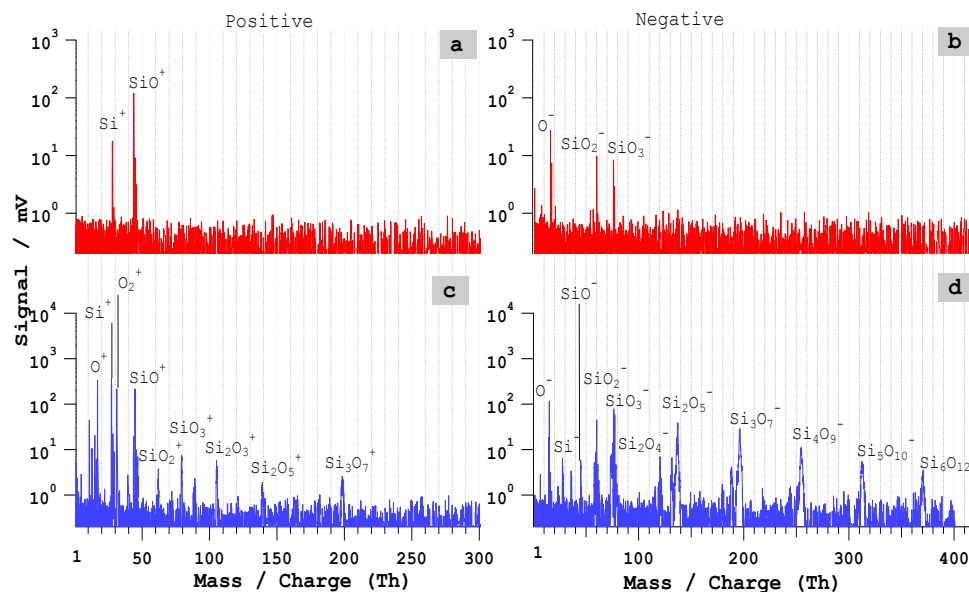
Figure 6: Bipolar mass spectra of SiO₂ single particles of d_P= 1100 nm. a – b: Typical ns-laser spectra; c – d: fs-LAAPTOF (λ = 800 nm) spectra.

Atmospheric
Measurement
Techniques
Discussions
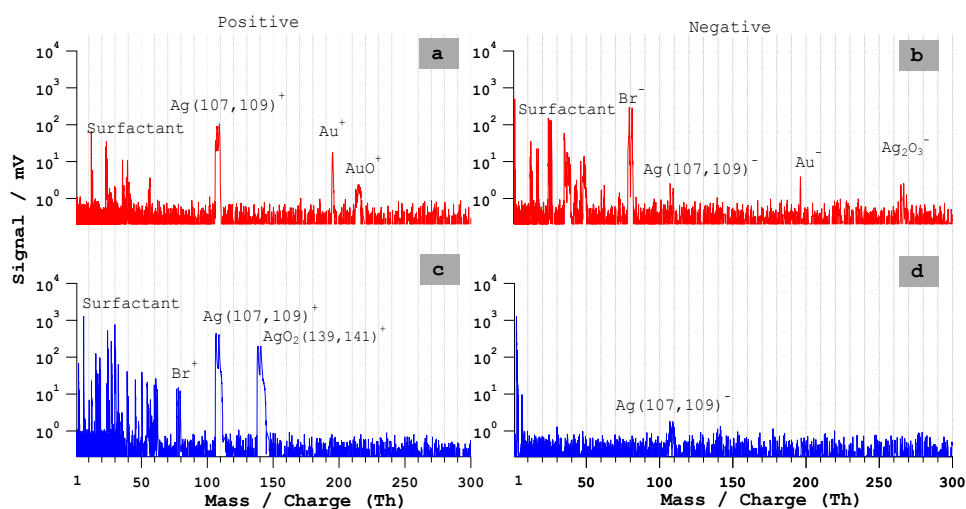
570   **Figure 7: Bipolar mass spectra of gold-silver core-shell particles of d_P= 600 nm. a – b: Typical ns-LAAPTOF spectra; c – d: fs-LAAPTOF (λ = 800 nm) spectra.**
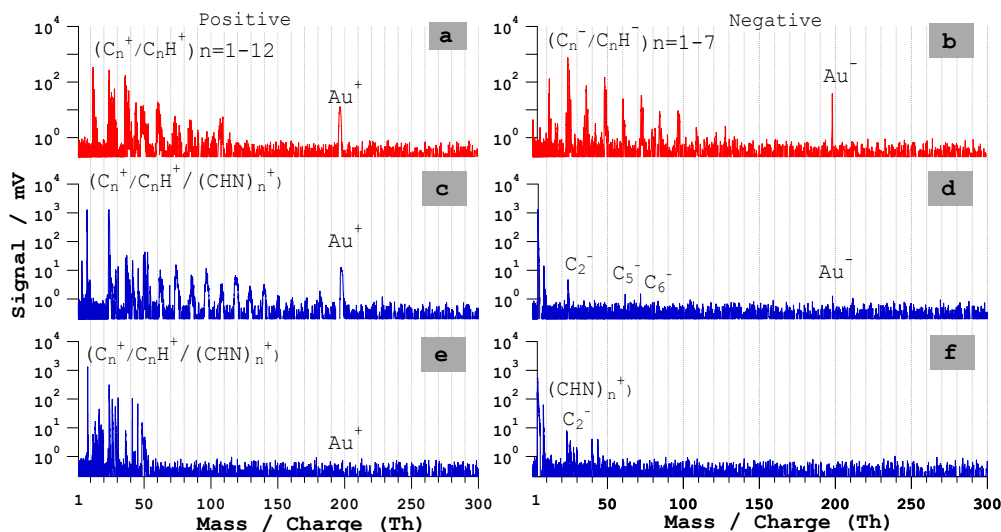
Figure 8: Bipolar mass spectra of Au-PAH core-shell particles. a – b: Typical ns-LAAPTOF spectra; c – d:
575   **fs-LAAPTOF (λ = 800 nm) spectrum that contains both gold and PAH signal, e-f: fs-LAAPTOF (λ=800 nm) spectrum without gold signal.**
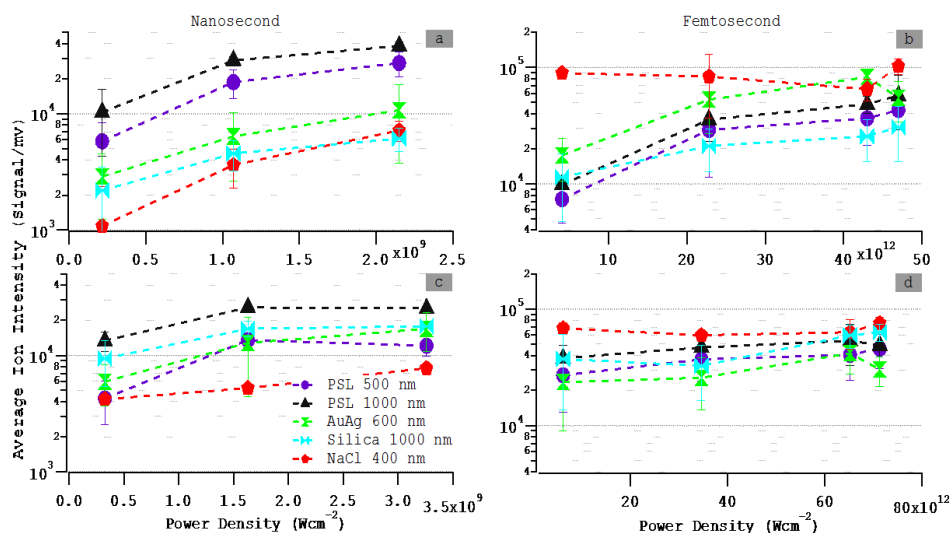
Figure 9: Variation of average ion intensity versus laser power density for different particle types. (a) Excimer laser, (b) fs-laser, focus position F1, (c) – (d) focus position F2.
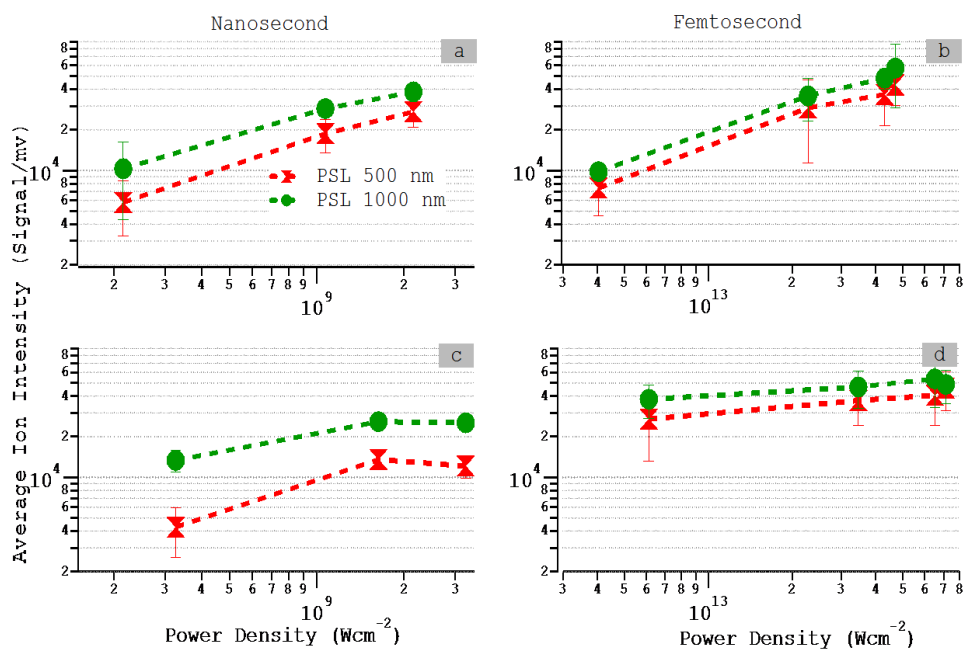
Figure 10: Variation of average total ion intensity with respect to size of PSL particles (500 nm, red circles, and 1000 nm, green triangles). (a, b) at focus position F2 and (c, d) at focus position F1.